

Final Draft
of the original manuscript:

Feistauer, E.E.; Bergmann, L.A.; dos Santos, J.F.:

Effect of reverse material flow on the microstructure and performance of friction stir welded T-joints of an Al-Mg alloy.

In: Materials Science and Engineering A. Vol. 731 (2018) 454 - 464.

First published online by Elsevier: June 20, 2018

DOI: 10.1016/j.msea.2018.06.056

<https://dx.doi.org/10.1016/j.msea.2018.06.056>

Effect of reverse material flow on the microstructure and performance of friction stir welded T-joints of an Al-Mg alloy

E. E. Feistauer, L. A. Bergmann*, J.F. dos Santos

Helmholtz-Zentrum Geesthacht, Centre for Materials and Coastal Research, Institute of Materials Research, Materials Mechanics, Solid State Joining Processes, Geesthacht, Germany

luciano.bergmann@hzg.de

Abstract

Friction stir welding (FSW) has been developed and commercially applied with success to connect large and complex structures. However, process optimization is still required to improve the mechanical performance of the T assemblies. Therefore, a second welding pass was applied in this work and was performed backwards, while maintaining the same tool rotation direction. Thus, due to the creation of a reverse material flow, a second advance side over the previously retreating side of the joint was formed, which significantly reduced the defects typically found in FSWed T-joints. The joints were manufactured with dissimilar Al-Mg alloys (AA5083), which is of particular interest to the shipbuilding sector. The microstructural analysis revealed that the second pass significantly reduced the kissing bonding defect on the joints retreating side. As a result, the mechanical properties were improved under quasi-static loading, reaching performance levels comparable to those of the base material. A digital image correlation system (DIC) linked to a tensile test system was used to investigate the local strain fields of the T-joints under two different loading conditions. The fatigue strength was also evaluated and the FSWed T-joints reached the fatigue keen with a nominal load range of 88.4 MPa under skin loading.

Keywords: T-joints, friction stir welding, joint mechanical properties, digital image correlation system.

1. Introduction

The transportation sector is faced with demands to systemically reduce the weight of its structures, to decrease greenhouse gas emissions and to provide more fuel-efficient vehicles. Furthermore, all stages of manufacturing must consider and comply with strict environmental requirements. Recent environmental policies have driven the development of advanced lightweight materials, lightweight designs, and manufacturing technologies[1,2]. These developments include the increasing application of multi-materials and lightweight alloys such as aluminium, magnesium, and titanium in the aerospace, automotive and shipbuilding sectors.

Recent welding technologies, such as friction stir welding (FSW), have been developed and commercially applied with success to connect large and complex lightweight structures for the transport sector. The advantages of FSW designs include the production of structures with excellent mechanical properties, the efficient consumption of energy, and a decrease in distortion, residual and thermal stresses, which result from a solid-state based welding process[3–5]. Moreover, FSW is completely automated, allowing a tight tolerance and precise control during the process to be achieved, which reduces the levels of reworking and minimizes the operation costs.

The FSW process has also been considered to manufacture strengthened aluminium panels formed through T-connections, which are able to increase the stiffness and inertia of skin plates without large increases in structural weight[6]. These joint configurations are typically applied in decking and hull areas of high-speed craft, lightweight ships, and aircraft fuselages.

The weldability of T-joints by FSW has been investigated by the scientific community and research institutes leading to the proposal of two different welding approaches. The first method, based on stationary shoulder friction stir welding (SSFSW), was introduced by TWI[7] and inserts the welding tool on the internal corner of the T-assembly forming a corner fillet weld. In contrast, the second approach inserts the tool tangential to the upper plate of the T-connection. Due to the tool complexity and clamping system required to produce fillet welds by the SSFSW, the second approach is preferred. However, the formation and distribution of welding defects such as kissing bonds, tunnels and oxide lines are commonly observed on the retreating side of the joints [8]. These defects are mostly a result of an asymmetric flow of plasticized material developed during the welding process[9–11].

Several different T-joints assemblies have been proposed in the literature. Tavares *et al.* presented at least six possible assemblies based on the position of the skin and stiffener plates[12]. In their work, a three-part assembly was chosen, and dissimilar T-joints were produced[12,13]. However, the process optimization was recommended by the authors, which aims at improving the joint mechanical properties. Cui L. and co-workers[14] manufactured AA6061-T4 T-joints by FSW in three different configurations and evaluated the defect formations during the process. Despite successfully producing welds in the three proposed assemblies, the joints presented defects at the internal corners. These defects were attributed to the initial position of the plates, insufficient heat generation and material flow patterns. The sensibility to defect formation was also reported by Fratini during the production of T-joints in AA6082[15,16], in which the joints' mechanical properties were evaluated and compared with extruded T-parts and MIG T-joints using a customized bending test. Buffa and collaborators[17,18] also reported material flow during the FSW of aluminium alloy T-joints by numerical simulations and experiments. The material flow on the skin plate was considered to be very similar to the FSW of butt joints, particularly in the skin plate. A thin foil of brass as a marker at the interface skin/stiffener was used to verify that the actual bonding surfaces between the two plates presented a wavy distribution. Additionally, they noted that the stirring action is more pronounced in the advancing side.

Different aspects of T-joints produced by FSW have been addressed, such as the process parameters[6], the tool geometry[19] and the shape of the corner fillet zones[20]. However, the highly heterogeneous local mechanical properties of the joints, long-term degradation and behaviour under cyclic loading are still knowledge gaps in the literature. The missing data must be taken into consideration when designing a structural T-connection, as well as the microstructural features resulting from the asymmetric temperature and material flow during FSW and its effects on the local and global mechanical properties of the structure.

In this paper, T-joints were produced by FSW with a 6 mm thick Al-Mg alloy, which is of particular interest to the shipbuilding sector. To overcome the defect formation due to the asymmetric flow of material during FSW, a second welding pass was applied. The joints were characterized by quasi-static and dynamic mechanical tests, and a digital image correlation system (DIC) linked to the tensile test system was used to investigate the local strain fields. Furthermore, the fatigue properties of the T-joints were investigated under two different loading conditions.

2. Experimental procedure

2.1. Production of welded samples

The T-joints were produced with cold rolled AA5083-H111 aluminium alloy (6 mm thickness) measuring 300 x 1000 mm as a skin plate and a 200 x 1000 mm stiffener plate. The base materials mechanical properties, standard chemical compositions[21] and those obtained by in-house analysis are presented in Table 1. The T-joints were welded by FSW in a two-pass approach, which consisted of a backward application of a second welding pass over a conventional FSW process, while maintaining the same tool rotation direction, as shown schematically in Fig. 1 (a). Therefore, due to a reverse material flow, a second advance side over the previously retreating side of the joint is created. The welding tool geometry consisted of a threaded conical pin (8 mm diameter) with three flats and a spiral shoulder with a diameter of 30 mm. Fig. 1 presents a schematic view of the welding approach (Fig. 1(b)) and the clamping system that was used (Fig. 1(c)). Two corner fillets of 3 mm radii were produced on the backing bar die plate to guarantee a smooth transition between the skin and the stiffener (Fig. 1(b)). The process parameters and the tool geometry used in this work are provided in Table 2.

Table 1: Chemical compositions and selected mechanical properties of the AA5083-H111.

	Weight %	Si	Fe	Cu	Mn	Mg	Cr	Zn	Ti
Chemical composition	Standard[21]	<0.4	<0.4	<0.1	0.4-1	4-4.9	0.05-0.25	<0.25	<0.15
	Test result	0.118	0,306	0,073	0,550	4,89	0,073	0,126	0,011
Mechanical properties	Loading direction		Rp0.2 [MPa]		Rm [MPa]		A [%]		
	PRD		145.1 ± 2.3		318.1 ± 0.4		21.3 ± 0.9		
	TRD		180.0 ± 0.3		358.4 ± 1.5		21.8 ± 1.2		

PRD – parallel to the rolling direction; TRD - transversal to the rolling direction

Table 2: Welding parameters and tool geometry.

Weld	n [rpm]	F_a [kN]	v [mm/s]	Tool geometry		
				Ø Shoulder	Ø Probe	L [mm]
First pass	600	25	6			
Second pass	600	25	6	30	8	7

n = rotational speed, F_a = axial force, v = welding speed, L= probe length

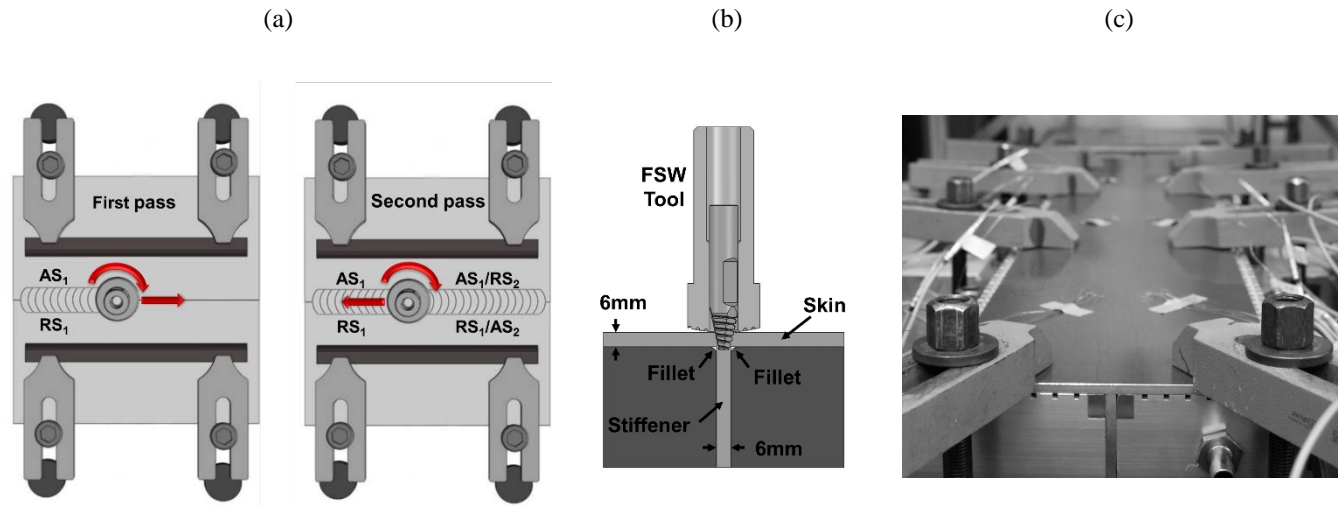


Figure 1: Schematic view of the welding approach and tool sketch (a), clamping system (b) and schematic top view of the first and second welding passes (c).

2.2. Process analysis

The welding machine used was an FSW Gantry System developed specifically by Helmholtz-Zentrum Geesthacht in cooperation with H.Loitz-Robotik GbR. The Gantry system allows the precise monitoring of the welding parameters, such as the forces applied across the spindles on the three axes, the torque applied by the tool, the rotation speed and the transversal speed, which are recorded during the process and can be used for further post-welding evaluation.

The process temperature was measured by thermocouples located at three different zones in the skin (named zones 1, 2 and 3) and the stiffener (T1, 2 and 3), as shown in Fig. 2. Each skin zone had six thermocouples installed, three of which were placed at the advancing side, and three were placed at

the retreating side. For the stiffener temperature measurement, one thermocouple per zone was installed and shifted 10 mm from the skin plate. All thermocouples were inserted 3 mm deep into the aluminium plates. The data acquisition was performed by a data acquisition system NI CompactDaq from National Instruments, which consists of a portable platform that integrates thermocouple sensors (type K), a measuring module and a PC.

2.3. Microstructure characterization

Cross-sectional specimens cut from the welds were mounted, ground, and polished up to 0.05 μm using a colloidal silica suspension. The weld microstructural features were analysed using an optical microscope with 90° polarized light from Leica, and an integrated digital camera was used to capture the microstructure of the samples. The microstructural features were revealed by electrochemical etching using Baker's reagent.

2.4. Assessment of mechanical properties

The T- joint mechanical performance was evaluated at local and global scales with quasi-static and cyclic loading tests. In terms of local mechanical properties, the cross-sectioned samples were subjected to the micro-hardness test. The indentations were carried out using a Zwick/Roll ZHV microhardness machine, and a 0.2 kgf load was applied for 10 seconds, according to the [ASTM E 384](#). This equipment has a fully automated x/y-table, and two indentation lines with a 40 mm length and the stir zone at the centre were produced on the cross-sectioned specimen. The first line was performed 2 mm below the skin surface edge, and the second line was shifted vertically 2 mm from the first one. The indentation lines were measured after each welding pass, and the distance between each indentation was 0.5 mm.

To understand and assess the deformation behaviour on the local scale, a digital image correlation system (DIC) linked to the tensile test machine was used, and strain maps were generated during the quasi-static tests. The samples were prepared according to GOM specifications and pictures of the samples were acquired by a 4-MP camera (50 mm focal length) for the duration of the tensile and pull-out tests with trigger signals being sent every second. The data management of the entire measurement, evaluation, and documentation was carried out with the integrated ARAMIS software.

Further investigations on the global scale were carried out using the quasi-static and cyclic loading tests. The specimen geometries are presented in Fig. 3 (a). The quasi-static loading was applied under two different loading directions. The first direction was loading the skin plate, and the second was pulling-out the stiffener plate. The sample geometries were based on the [ASTM: E8M](#) standard. For

the stiffener pull-out testing, a half dog-bone shape was produced by EDM, following the ASTM geometry, as shown in Fig. 3 (a). The tests were performed at room temperature using a Zwick/Roell universal testing machine with a load capacity of 100 kN and a constant crosshead speed of 1 mm/min.

Within the framework of cyclic loading, the fatigue endurance was assessed by the fatigue tests, and the specimen geometries, based on the ASTM standards ([ASTM: E466](#)), are presented in Fig. 3 (b). The clamping systems used during the tests are shown in Fig. 4. Following the same approach adopted for the quasi-static loading, the tests were performed under the two different loading conditions of loading the skin in the first scenario (Fig. 4 (a)) and pulling out the stiffener in the second scenario (Fig. 4 (b)). The tests were performed under a stress ratio of 0.1 using a servo-hydraulic fatigue test machine. In total, for each test configuration, 21 welded specimens were tested, and the fatigue endurance was defined as a stress level below which no failure would occur after 6×10^6 cycles. All tests were carried out with a frequency of 40 Hz.

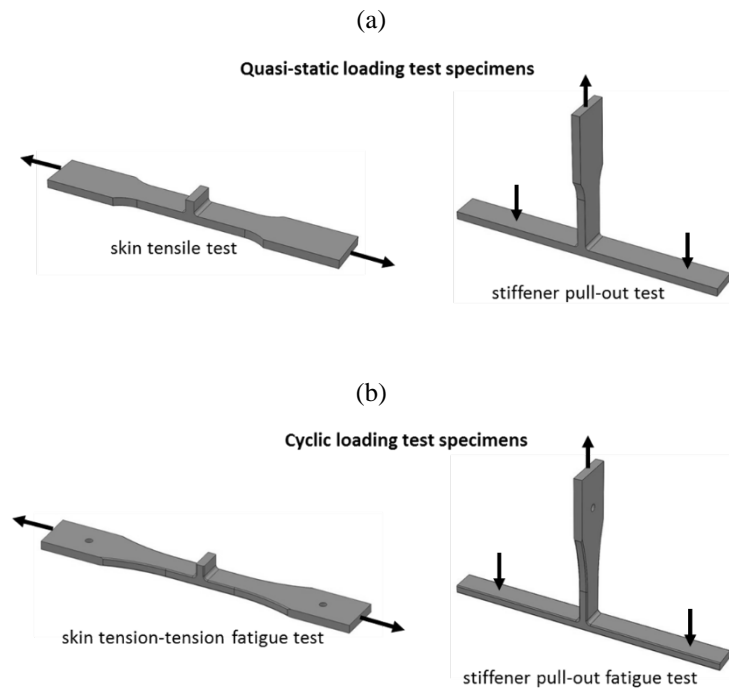


Figure 3: Specimen geometries for the quasi-static (a) and cyclic loading tests (b).

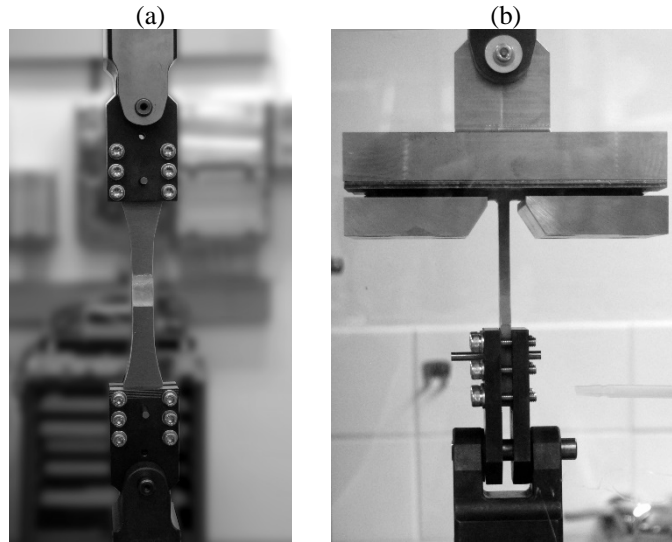


Figure 4: Clamping system for the fatigue tests, skin loading (a) and stiffener pull-out loading (b).

3. Results and discussion

3.1. Process evaluation

The spindle torque, tool rotational speed and force applied on the spindle were measured during the welding experiments and used to evaluate the process (Fig. 5). A typical FSW process diagram obtained by plotting of these data over the welding time is presented for the first welding pass in Fig. 5 (a). The torque (dark line) has an initial abrupt rise in its absolute value, which corresponds to the tool plunging phase. Then, the torque tends to follow a constant range of variation, resulting from the displacement of the tool while welding. At the final step, the tool displacement is stopped, and the tool is retracted, which results in the torque value rapidly decreasing to values near zero. The force applied on the spindle presents a very similar behaviour as shown by the light grey line of the process diagram.

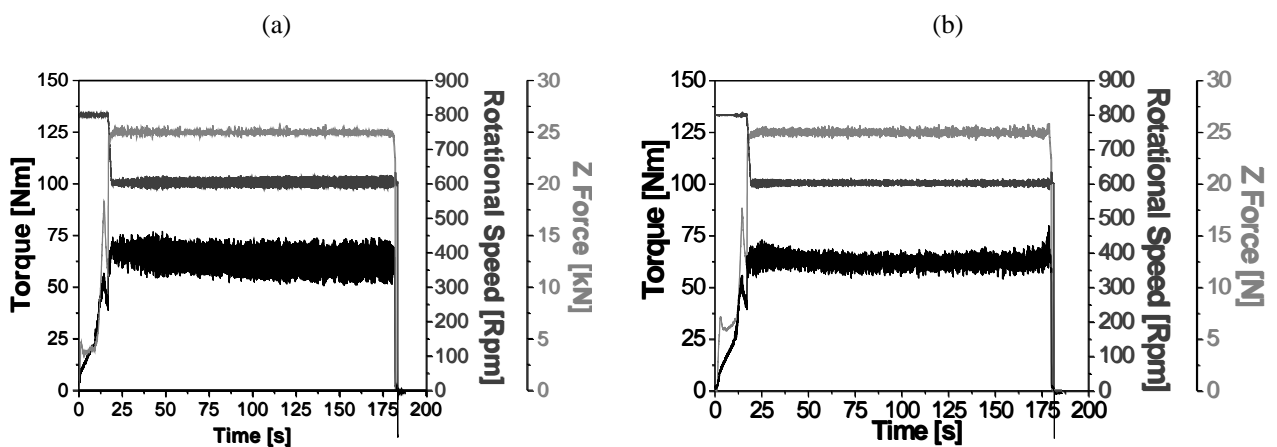


Figure 5: Process diagrams for the first (a) and second welding passes (b).

Two different steps for the rotational speed were used during the welding. Firstly, during the plunging phase, the tool begins to rotate at 800 rpm but decreases to 600 rpm as soon as it starts to move forward (Fig 5. (a) dark grey line). This procedure intends to rapidly plasticise the material below the tool, thereby facilitating the tool insertion in the materials to be welded without damage the tool probe.

During the second welding pass (Fig. 5 (b)), which was applied backwards while keeping the same rotational speed (600 rpm) and direction of the first pass, a more stable regime of torque variation was observed. This may be a result of the smoother welding from the re-welding process, as opposed to creating a new weld. As a result, the average torque measured from the stable regime tends to be slightly lower than the one measured in the first pass, as well as the power and, consequently, the calculated heat input, as presented in Table 3.

Table 3: Process parameters.

Weld	Torque [Nm]	Power [W]	Heat input [J/mm]
First pass	66.3	4163.8	624.6
Second pass	63.5	3989.8	598.5

Fig. 6 presents the results of the temperature measurements for the first (Fig. 6 (a)) and second (Fig. 6 (b)) welding passes. The results are plotted in terms of the average values from the three zones of measurement. Due to the asymmetric temperature fields created during the FSW[3,22], a slight difference between the maximum temperature recorded in both welding sides was observed. However, this asymmetry tends to be less pronounced as the tool travels along the weld. The highest temperature measured was 321.9 °C at the advancing side of the first welding pass (AS₁), as shown in Table 4. In accordance with the heat input estimation, the temperature measured in the second pass was slightly lower compared to the first one, especially when the average values obtained for the first advancing side (A₁) are compared to the second side (RS₁/AS₂). However, the standard deviation was on the same order of magnitude as the observed differences.

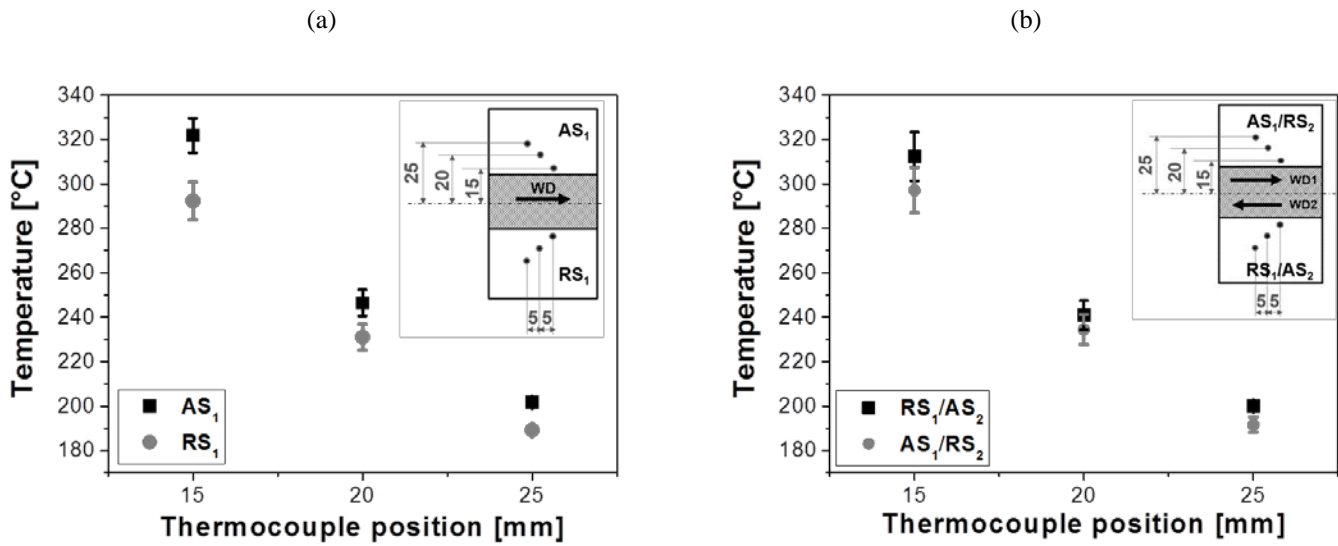


Figure 6: Temperature measurements for the first (a) and second welding passes (b). The presented temperature values correspond to the average values of the thermocouples placed at the same distance from the welding line in the three zones.

Table 4: Maximum temperature reached during welding.

Thermocouples	Maximum temperature (°C)				
	Skin			Stiffener	
	15 mm	20 mm	25 mm		
First pass	AS ₁	321.9 ± 7.8	246.5 ± 6.0	201.7 ± 1.3	236.8 ± 12.9
	RS ₁	292.3 ± 8.5	231.1 ± 5.9	189.3 ± 1.1	
Second pass	RS ₁ /AS ₂	312.3 ± 11.0	240.9 ± 6.5	200.0 ± 1.2	238.7 ± 6.2
	AS ₁ /RS ₂	297.1 ± 10.2	234.5 ± 6.7	191.6 ± 3.4	

3.2. Microstructural features

The combination of the high process temperature (measured T_{max} was 321.9 °C) and intense plastic deformations induced by the tool stirring movement during the FSW produce significant variations in the microstructures of the welded T-joints, as shown in the cross-sectional analysis of Fig. 7. To fill the cavities formed between the corner fillet and the aluminium plates, material from the upper plate must flow downwards. As a result, a slight thickness reduction in the skin plate was observed, and a rounding transition between the skin and the stiffener was formed.

As reported by several authors[9–11,20], a kissing bond is typically formed at both of the corner fillets of the friction stir welded T-joints, which tends to be more pronounced at the retreating side after the first welding pass, as observed in Fig. 7. This asymmetric distribution of defect can be associated with the asymmetric plastic deformation induced by the rotational movement and translation of tool during the FSW. The kissing bond defect is composed by oxide particles present on the unwelded material surface, which remains at the fillets zones between the skin and stiffener due to insufficient mechanical mixture[20], although it normally experiences intense plastic

deformations. Therefore, it typically presents a wavy distribution as shown in Fig. 7 (a). The kissing bond was dispersed at the stir zone in the advancing side, due to more intense shear stress and plastic deformation. However, at higher magnifications, it could be observed that the defect is still present at the corner fillet where the stirring action was not sufficiently efficient, as indicated in Fig. 7(b) by the black arrow.

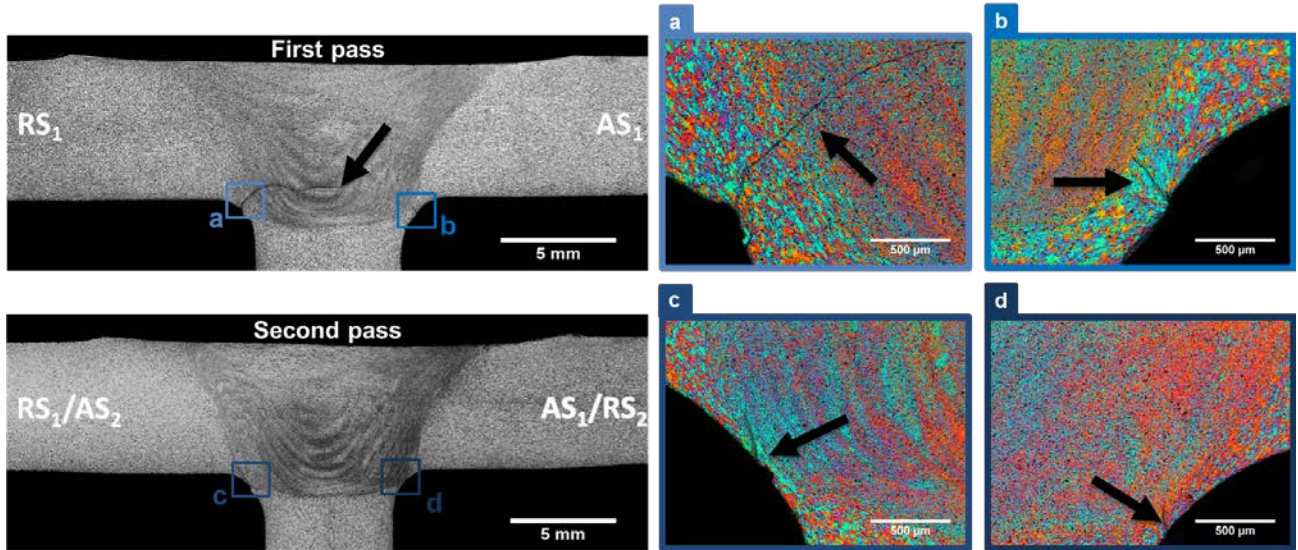


Figure 7: T-joint cross-sectional views after the first and second welding passes with detailed micrographs of the corner fillets after the first pass at the RS_1 (a), AS_1 (b) and after the second pass at the RS_1/AS_2 side (c) and AS_1/RS_2 (d).

The kissing bond defect was significantly reduced after the second pass, and it was not observed through the cross-sectional analyse presented in Fig. 7 (second pass cross-sectional view). However, its presence was confirmed at higher magnification, although much less pronounced, as shown in Figs. 7(c) and (d). After the second pass, the welding tool penetrated deeper into the skin plate due to the thickness reduction created by the previous welding pass. Consequently, it may contribute to increase in the stirring action close to the corners, which combined with the reverse material flow induced by the backwards motion of the tool (as described in Section 2.1.), efficiently disperses the kissing bond defect in both welding sides.

In addition, it was observed that the welding process intensely altered the microstructure of the central portion of the T-joint, which was entirely replaced by a fine-grained, equiaxed recrystallized microstructure, as shown in Fig. 8. However, the second welding pass did not produce significant changes in the SZ microstructure when compared with the joint produced with one welding pass. The comparison between the microstructure of the base materials and welded material after the first and second welding passes are shown in Figs. 8 (a), (b) and (c), respectively. The microstructural changes observed on the thermo-mechanically affected zone and the stir zone of the joints were similar to

those typically observed in Al-Mg alloys welded by FSW and have already been addressed by other authors[23,24].

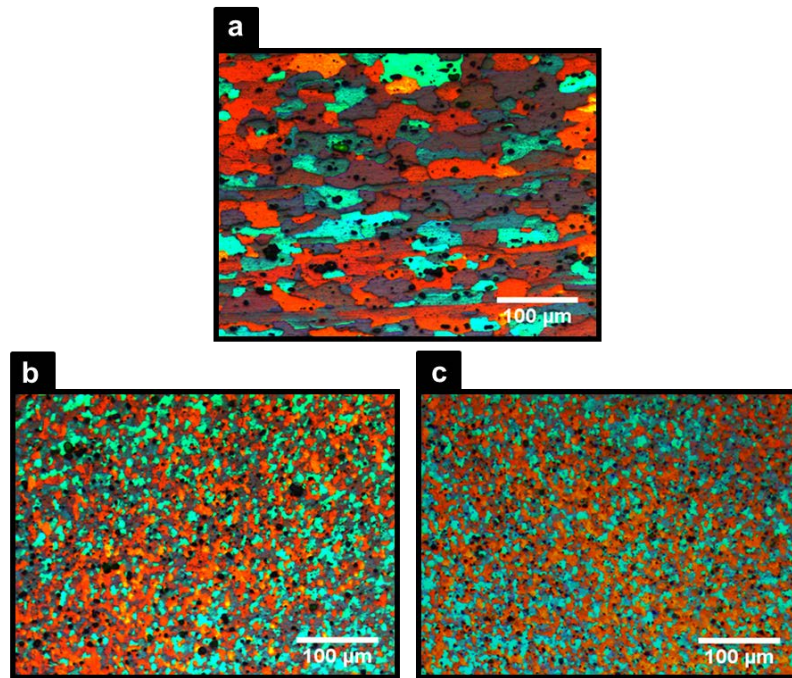


Figure 8: Microstructure comparison between the base material (a), the stir zone after the first (b) and second welding passes (c).

3.4. Microhardness profile

The microstructural changes caused by FSW, mainly at the SZ, as previously discussed, did not significantly influence the local mechanical properties of the T-joints. Microhardness evaluation of the cross-sectioned sample (Fig. 9) showed that the hardness values presented a constant range of variation between 67 and 83 HV (maximum hardness values measured in the SZ). However, one can identify a tendency of the hardness value to increase at the central portion of the joint, indicated in the shoulder contact area of the graphic. This could be associated with the formation of smaller dynamic recrystallized grains, which present greater grain edges and surfaces per unit of volume, as well as a higher dislocation density[5,23,24]. The application of a second welding pass resulted in the same tendency as observed for the first pass, and did not affect the local joint mechanical properties significantly. Such observation is in line with the microstructural characterization previously discussed. Therefore, it could be concluded that the grain size at the stir zone and microhardness are virtually unchanged by the induced reverse material flow during the second welding pass.

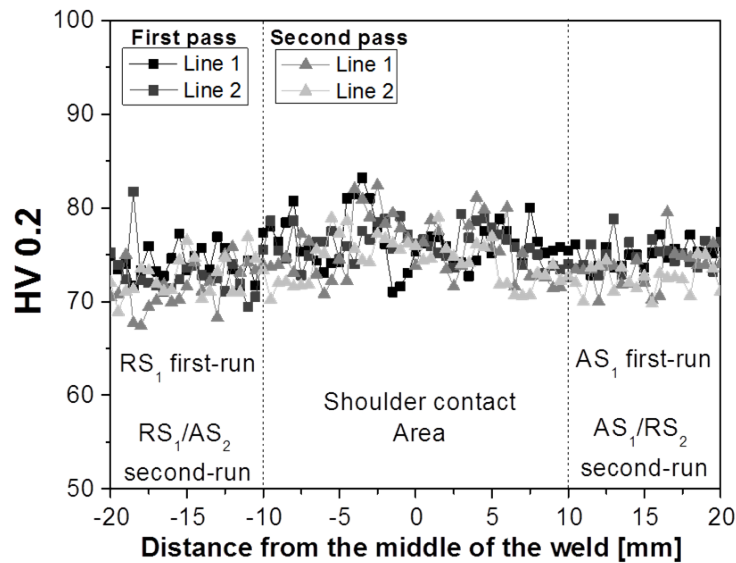


Figure 9: T-joint hardness profile after the first and second welding passes.

3.5. Mechanical properties under quasi-static loading

Fig. 10 (a) presents the comparison between the engineering stress-strain curves of the T-joints produced with one and two welding passes, which were obtained through the skin plate loading. Tensile properties were calculated using the nominal area of the skin plate (120 mm^2) to simplify the comparison between the two conditions. Both curves nearly overlap each other during the elastic deformation region. Therefore, the yield point was virtually the same for the joints produced with one ($R_{p0.2} = 142.3 \pm 7.3 \text{ MPa}$), and two welding passes ($R_{p0.2} = 140.3 \pm 4.1 \text{ MPa}$). However, for the second welding pass, the maximum strength and energy absorbed prior to failure increases significantly, which were $R_m = 291.0 \pm 7.3 \text{ MPa}$ and $A = 14.0 \pm 0.9 \%$, respectively, for the first pass and $R_m = 306.0 \pm 4.5 \text{ MPa}$ and $A = 17.7 \pm 5.5 \%$, respectively, for the second pass. The complete tensile test data are presented in Table 5. The serrated yielding that appears on the T-joint stress-strain curve (known as the Portevin-Le Chatelier effect) is a typical behaviour of Al-Mg alloys and has been described in detail in the literature[25,26].

The strain maps obtained under the tensile loading are presented in Fig. 10(b). The strain was heterogeneously distributed across the specimen and concentrated primarily at the kissing bond (at the retreating side) where the final failure took place for the single-pass joint. However, the reduced size of the defect created by the second pass displaced the strain concentration to the base material where the failure took place for the two-pass T-joint, justifying the increase in R_m and A as previously presented. Hence, the two-pass T-joint presented mechanical properties comparable to the base material.

Table 5: Mechanical properties obtained through the skin loading and stiffener pull-out tests.

	Skin loading test			Stiffener pull-out test
	Rp 0.2 [N/mm ²]	Rm [N/mm ²]	A [%]	F _{max} [kN]
First pass	142.3 ± 7.3	291.0 ± 7.3	14.0 ± 0.9	22.3 ± 1.3
Second pass	140.3 ± 4.1	306.0 ± 4.5	17.7 ± 5.5	32.6 ± 0.6

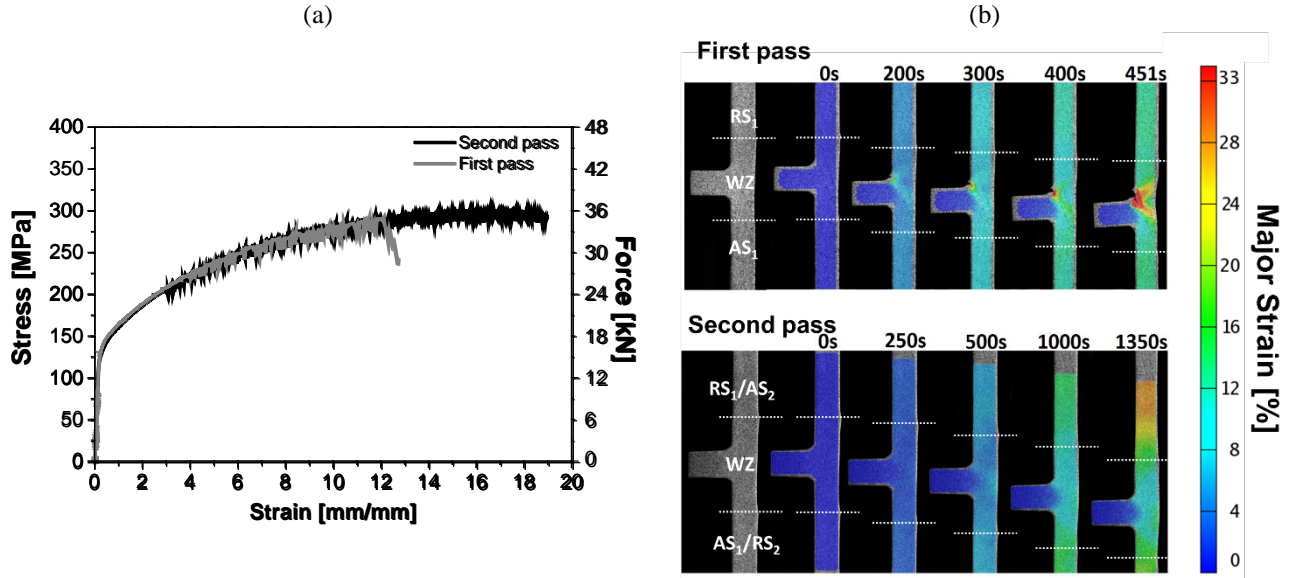


Figure 10: Tensile stress-strain curves of the skin loading test (comparison between replicates R1 after the first and second welding passes) (a) and strain maps resulting from the DIC measurements (b). In the far left mapping in (b) show a typical speckled black pattern contrast is shown applied over the T-joint lateral surface used for the DIC measurements.

The second welding pass displayed an even more positive effect on the joint strength and energy absorbed prior to failure regarding the stiffener loading, as shown in Fig. 11. The increase in force required to pull the stiffener from the T-joint was approximately 46% after the second pass, as shown in Table 5 (22.3 ± 1.3 and 32.6 ± 0.6 kN for the single and two-pass T-joint, respectively). Moreover, the second pass changed the failure mechanism of the T-joint under pull-out forces, as shown in the strain maps in Fig. 11 (b). In the single-pass joint, the failure was initiated at the very beginning of the test over the kissing bond at the RS and propagated through the SZ towards the corner fillet at the AS, thus pulling the stiffener plate out from the T-joint (Fig. 11 (b) first pass).

After the second pass, higher levels of deformation were observed, and a higher pulling force was required to start the failure. As a result, the strain concentration is primarily displaced to the skin plate, and no failure nucleation is observed. Therefore, the second welding pass results in more significant bending of the skin plate in comparison to the single pass case. Due to the strain being constrained by the support bars, further loading displaces the strain concentration to the joint fillet. Thus, it begins to open the kissing bond, and the failure propagates on the AS₁/RS₂ towards the skin plate, which breaks the first side of the joint (Fig. 11 (b)). Consequently, it generates an abrupt decrease of the pull-out force, as observed in the pull-out force versus displacement curves in Fig. 11

(a). The load-bearing capability of the joint is necessarily affected by the first break, which now is held only by a single side. While the displacement is constant during the test, the remaining side of the joint is quickly overloaded, and the failure takes place close to the support bar, as shown in Fig. 11(b) for the second pass.

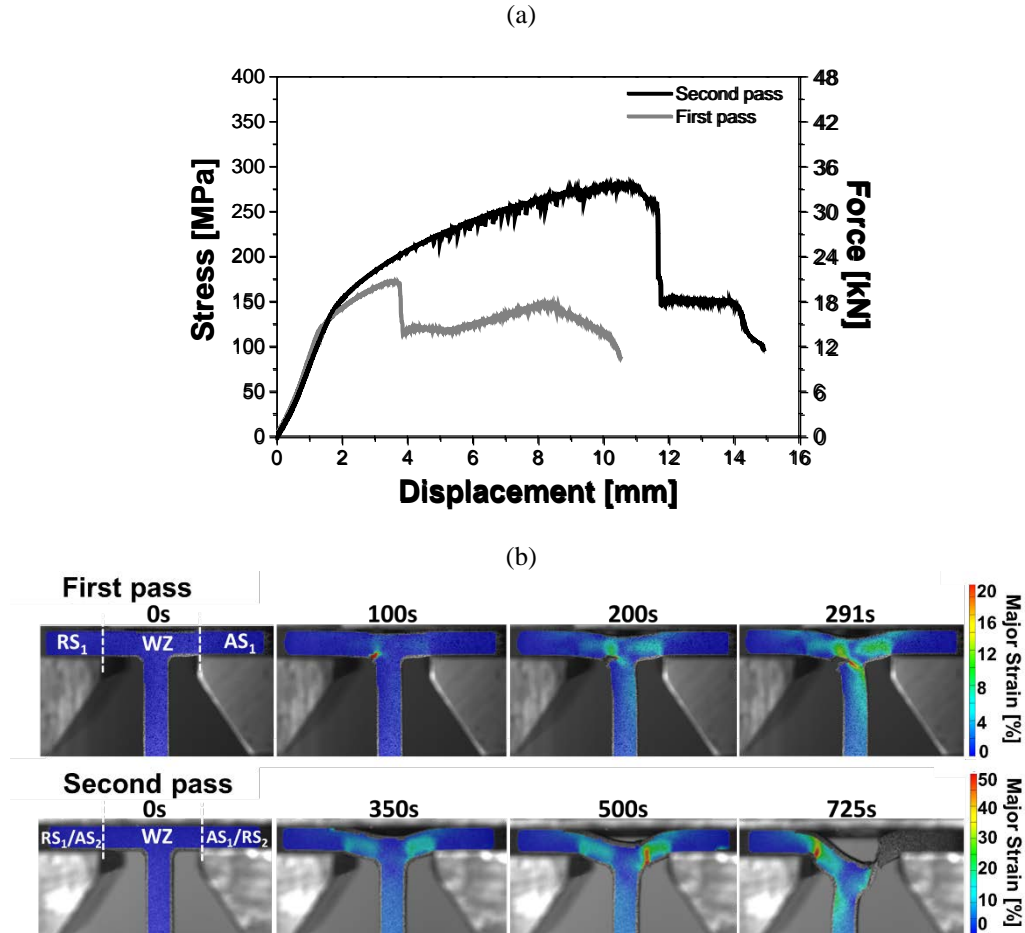


Figure 11: Pull-out force versus displacement curves obtained from the stiffener loading (a) and strain maps resulting from the DIC measurements (b).

3.6. Fatigue properties

The Wöhler curves obtained for the as-welded two-pass T-joint under the skin and stiffener loadings are shown in Fig. 12 (a). To assess and compare the fatigue data, both curves were plotted with respect to the nominal stress range ($\sigma_{\max} - \sigma_{\min}$) and taking into consideration only the nominal area of the base plates. The complete test parameters for each tested specimen are presented in Table 5. The joints were tested under seven load conditions from L0 to L6 and for each one of the three replicates tested. The two-pass joint reached the fatigue endurance at a maximum load of 88.4 MPa under skin loading and 28.4 MPa under stiffener loading. As expected, the stiffener loading results in a lower fatigue strength since the loading direction tends to open the kissing bond easily. Thus, lower energy is required to initiate a crack through the welded area.

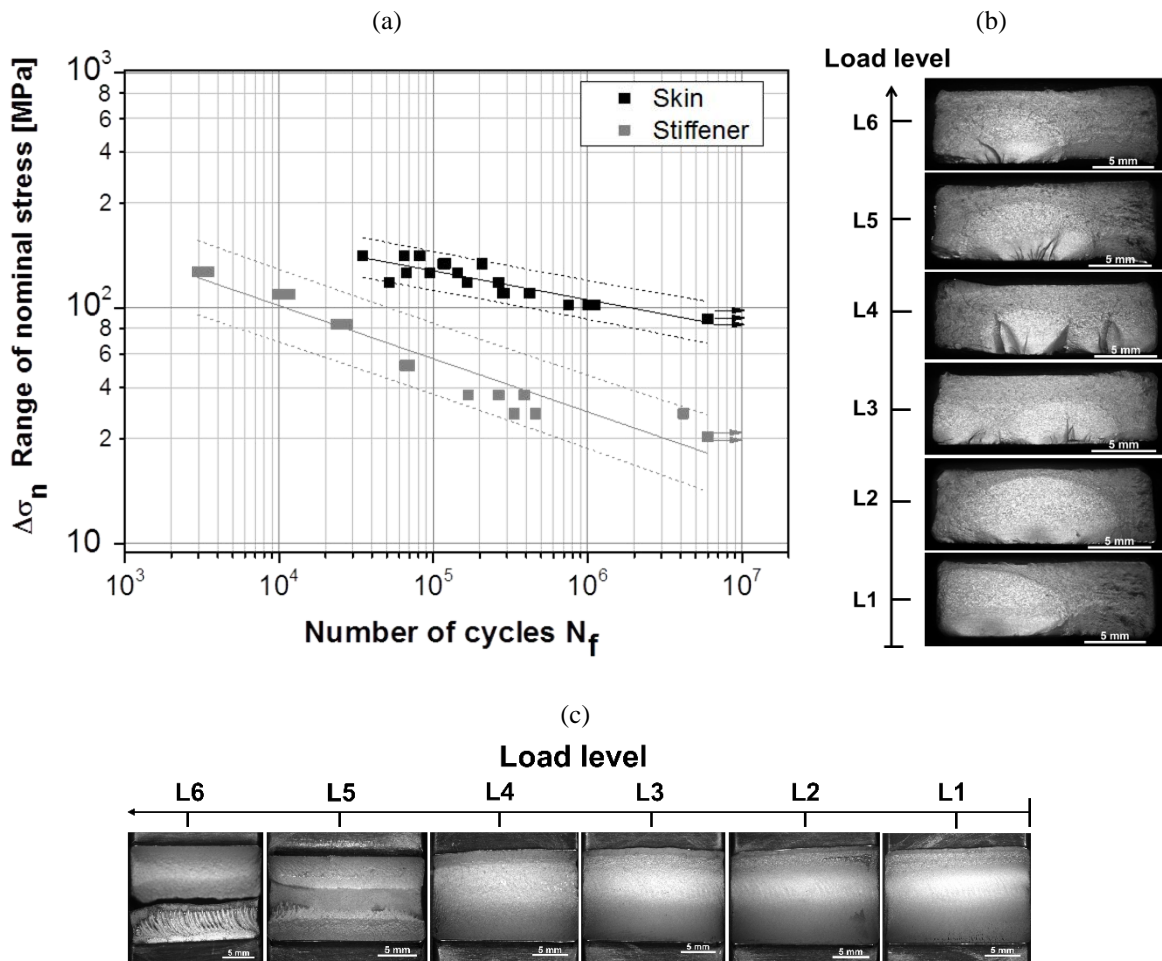


Figure 12: Wöhler curve for the T-joints under skin and stiffener loading (a), fractographic resultant from each load condition for the skin (b) and stiffener (c).

The marks led by the tool on the T-Joint surface, combined with the thickness reduction on the welded zone (as shown in Fig. 7), act as a favourable crack initiation site under skin loading. Consequently, fractures occurred at the T-joint corners starting on the skin surface as shown in Fig. 13 (a). However, a different behaviour was observed for the stiffener loading, as previously described and as shown in Fig. 13 (b). The fracture surfaces of each load condition are illustrated in Figs. 12 (a) and (b).

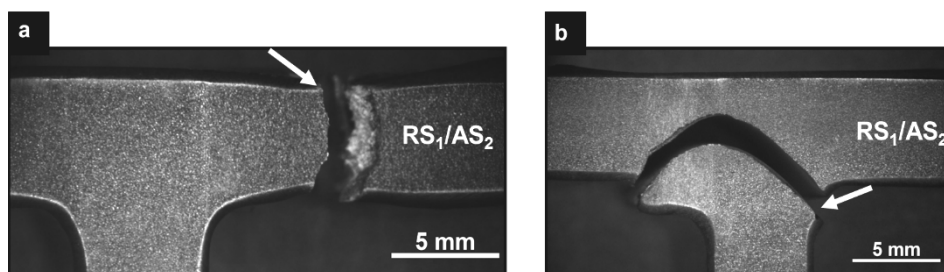


Figure 13: Fatigue failure location for samples tested under skin (a) and stiffener (b) loading.

Regarding skin loading, the observed morphological characteristics on the fracture surface (Fig 12 (b)) were similar to those typically observed in fatigue-tested specimens, and different regions related

to the crack initiation, propagation, and final fracture were observed, which will be addressed in detail next. Moreover, multiple crack initiation sites were observed in the specimens where a high range of nominal stress was applied, as clearly identify for the specimen tested under load levels L5 and L4 of Fig 12 (b). However, different fracture morphologies were observed after the stiffener had been pulled out, especially at high levels of range of nominal stress (L6 and L5, Fig. 12 (c)). At these tests conditions, the fracture occurs similarly as previously reported under quasi-static loading (see strain maps of Fig. 11), exposing the joint stir zone, and the stirring flow pattern as shown by the macroscopic examination in Fig. 12 (c) - L6.

Table 6: Fatigue experimental data.

Load level	Samples	Skin			Stiffener		
		ΔF (kN)	$\Delta\sigma$ (MPa)	Cycles	ΔF (kN)	$\Delta\sigma$ (MPa)	Cycles
L6	R1	16.7	164.2	64520	14.3	140.2	3263
	R2	16.7	164.2	81676	14.3	140.2	3528
	R3	16.7	164.2	34893	14.3	140.2	2964
L5	R1	15.5	151.5	94967	11.4	111.8	11826
	R2	15.5	151.5	66775	11.4	111.8	9801
	R3	15.5	151.5	144272	11.4	111.8	10406
L4	R1	14.2	138.9	207203	8.6	84.3	23369
	R2	14.2	138.9	119639	8.6	84.3	26345
	R3	14.2	138.9	116038	8.6	84.3	27936
L3	R1	12.9	126.3	265069	5.7	55.9	70164
	R2	12.9	126.3	51988	5.7	55.9	67934
	R3	12.9	126.3	165585	5.7	55.9	65513
L2	R1	11.6	113.7	279961	4.3	42.2	388433
	R2	11.6	113.7	419850	4.3	42.2	264193
	R3	11.6	113.7	288858	4.3	42.2	167604
L1	R1	10.3	101.0	1108472	3.6	35.3	459426
	R2	10.3	101.0	748060	3.6	35.3	334500
	R3	10.3	101.0	1005870	3.6	35.3	4164953
L0	R1	9.0	88.4	6000000	2.9	28.4	6000000
	R2	9.0	88.4	6000000	2.9	28.4	6000000
	R3	9.0	88.4	6000000	--	--	--

3.7. Fracture surfaces

To further understand the failure under cyclic loading, the micromechanisms of the fracture were assessed by SEM, and the results are presented in Fig. 14 for the skin loading and Fig. 15 for the stiffener. The samples with higher fatigue life were selected for these analyses (L1 for each condition). Despite some differences in the features at the macroscale, the micromechanisms of the fractures for the two tested conditions are relatively similar, differentiated by only the crack initiation regime.

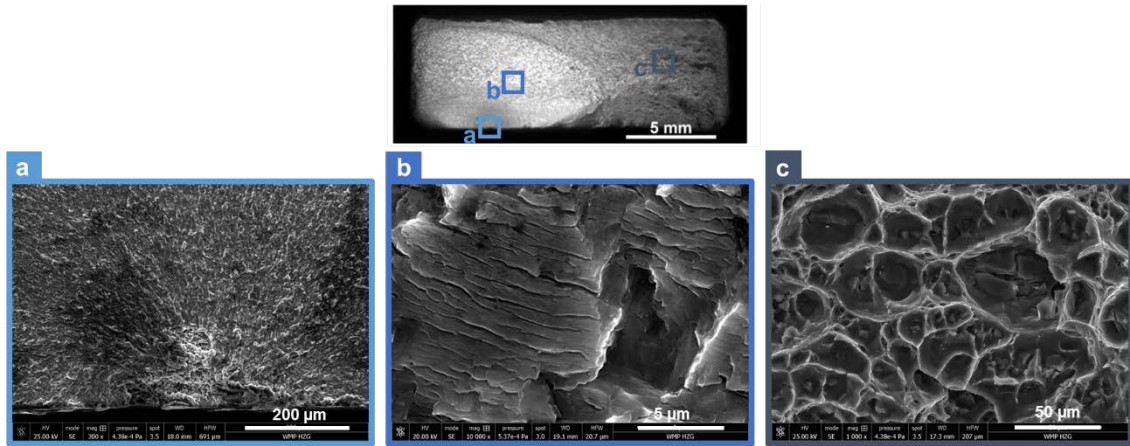


Figure 14: SEM micrographs of the skin loading test showing the fatigue initiation sites (a), crack propagation zone (b) and fast crack growth region (c).

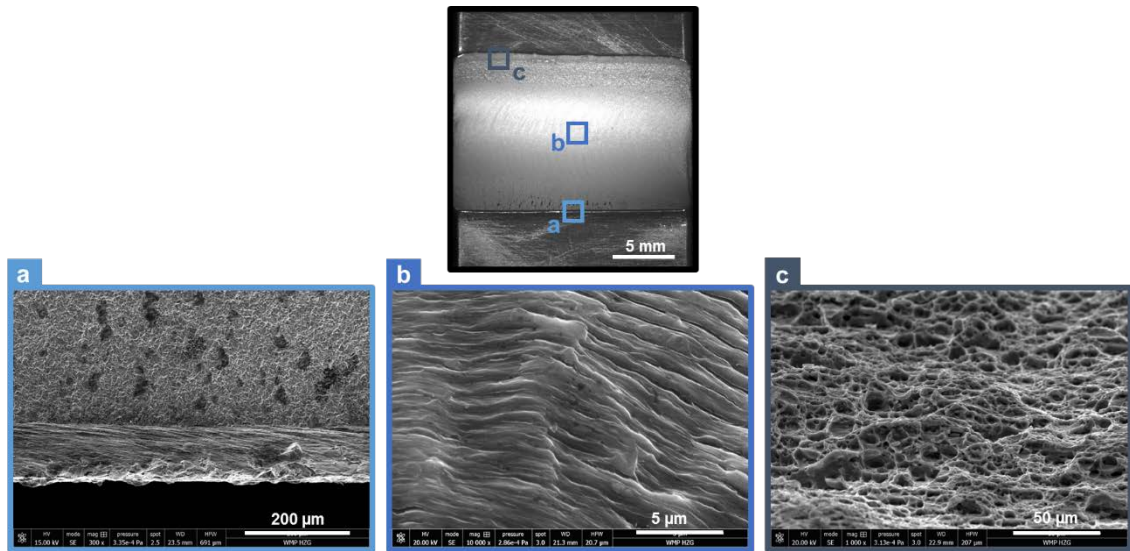


Figure 15: SEM micrographs of the stiffener loading test showing the fatigue initiation sites (a), the crack propagation zone (b) and the fast crack growth region (c).

Due to the low-stress levels, the joint tested under skin loading features a single crack initiation site, as shown in Fig. 14 (a). The stable crack growth regime exhibits parallel fatigue patches characterized by fine fatigue striations, detailed in Fig. 14 (b). During this stage, the crack propagated along multiple plateaus that are at different elevations, indicating plastic deformation during the crack growth at microscale. Once the fatigue crack reaches a critical size, it becomes unstable, and the crack growth rate increases catastrophically. The fast fracture of the T-joint was characterized by very ductile behaviour and thus displays a large number of variously shaped dimples. Similar zones of crack propagation (Fig. 15(b)) and final fractures (Fig. 15 (c)) were observed for the stiffener fracture surface. However, the cracks initiate at the kissing bond and display a flat surface (Fig. 15(a)).

4. Conclusions

The influence of a second welding pass on the mechanical properties of the friction stir welding process of T-joints produced with 6 mm thickness cold rolled AA5083 was evaluated. Based on the presented results, the following conclusions can be drawn:

- The second welding pass was applied backwards while maintaining the same tool rotation direction, creating a reverse material flow. As a result, it increased the material mixture and significantly reduced the kissing bond, especially at the retreating side from the first welding pass.
- Process analysis revealed that during the second pass, the process was more stable in comparison with the first pass, resulting in lower torque variation during welding.
- Mechanical properties of the T-joints were significantly affected by the second welding pass, which improved the joint performance under the skin tension and stiffener pull-out loading.
- DIC strain maps showed the displacement of the strain concentration from the corner fillet to the base material after the second pass, where the fracture occurred during the skin loading test. Thus, the energy absorbed prior to failure increased considerably after the second pass for both loading cases.
- The two-pass T-joint reached the fatigue endurance with a nominal stress load of 88.4 MPa under skin loading and 28.4 MPa under stiffener loading. The fracture occurred on the skin plate for the first loading case, due to a combining effect of the marks led by the tool on the surface and the local reduction of the area caused by the material that flowed to fill the joint fillets. In the second loading case, the fracture began on the kissing bond and propagated through the stir zone.

Acknowledgments

The authors would like to acknowledge the financial support provided to Eduardo E. Feistauer by the *Conselho Nacional de Desenvolvimento Científico e Tecnológico* - CNPq (Brazil).

5. References

- [1] H.E. Friedrich, Challenges of materials technology for low consumption vehicle concepts, *Adv. Eng. Mater.* 5 (2003) 105–112.
- [2] M. Redelbach, M. Klötzke, H.E. Friedrich, Impact of lightweight design on energy consumption and cost effectiveness of alternative powertrain concepts, in: *EEVC Eur. Electr.*

- Veh. Congr., Brussels, Belgium, 2012: pp. 1–9.
- [3] R. Nandan, T. DebRoy, H.K.D.H. Bhadeshia, Recent advances in friction-stir welding – Process, weldment structure and properties, *Prog. Mater. Sci.* 53 (2008) 980–1023. doi:10.1016/j.pmatsci.2008.05.001.
- [4] R.S. Mishra, P.S. De, N. Kumar, *Friction Stir Welding and Processing*, Springer International Publishing, Cham, 2014.
- [5] R.S. Mishra, Z.Y. Ma, Friction stir welding and processing, *Mater. Sci. Eng. R Reports.* 50 (2005) 1–78. doi:10.1016/j.mser.2005.07.001.
- [6] A.C.F. Silva, D.F.O. Braga, M.A.V. de Figueiredo, P.M.G.P. Moreira, Friction stir welded T-joints optimization, *Mater. Des.* 55 (2014) 120–127. doi:10.1016/j.matdes.2013.09.016.
- [7] J.P. Martin, C. Stanhope, S. Gascoyne, Novel Techniques for Corner Joints Using Friction Stir Welding, TMS 2011 Annu. Meet. Exhib. (2011).
- [8] J.S. Jesus, J.M. Costa, A. Loureiro, J.M. Ferreira, Assessment of friction stir welding aluminium T-joints, *J. Mater. Process. Technol.* 255 (2018) 387–399. doi:10.1016/J.JMATPROTEC.2017.12.036.
- [9] Y. Zhao, L. Zhou, Q. Wang, K. Yan, J. Zou, Defects and tensile properties of 6013 aluminum alloy T-joints by friction stir welding, *Mater. Des.* 57 (2014) 146–155. doi:10.1016/j.matdes.2013.12.021.
- [10] A. Astarita, A. Squillace, A. Scala, A. Prisco, On the critical technological issues of friction stir welding T-joints of dissimilar aluminum alloys, *J. Mater. Eng. Perform.* 21 (2012) 1763–1771. doi:10.1007/s11665-011-0073-3.
- [11] L. Cui, X. Yang, Y. Xie, X. Hou, Y. Song, Process parameter influence on defects and tensile properties of friction stir welded T-joints on AA6061-T4 sheets, *Mater. Des.* 51 (2013) 161–174. doi:10.1016/j.matdes.2013.04.013.
- [12] S.M.O. Tavares, P.C.M. Azevedo, B. Emílio, V. Richter-Trummer, M.A. V. Figueiredo, P. Vilaça, P.M.S.T. de Castro, Friction Stir Welding of T-Joints in Dissimilar Aluminium Alloys, (2008) 265–273. doi:10.1115/IMECE2008-67522.
- [13] S.M.O. Tavares, R. a. S. Castro, V. Richter-Trummer, P. Vilaça, P.M.G.P. Moreira, P.M.S.T. de Castro, Friction stir welding of T-joints with dissimilar aluminium alloys: mechanical joint characterisation, *Sci. Technol. Weld. Join.* 15 (2010) 312–318. doi:10.1179/136217109X12562846839114.
- [14] L. Cui, X. Yang, G. Zhou, X. Xu, Z. Shen, Characteristics of defects and tensile behaviors on friction stir welded AA6061-T4 T-joints, *Mater. Sci. Eng. A.* 543 (2012) 58–68. doi:10.1016/j.msea.2012.02.045.

- [15] L. Fratini, F. Micari, A. Squillace, G. Giorleo, Experimental Characterization of FSW T-Joints of Light Alloys, *Key Eng. Mater.* 344 (2007) 751–758. doi:10.4028/www.scientific.net/KEM.344.751.
- [16] L. Fratini, G. Buffa, L. Filice, F. Gagliardi, Friction stir welding of AA6082-T6 T-joints: process engineering and performance measurement, *Proc. Inst. Mech. Eng. Part B J. Eng. Manuf.* 220 (2006) 669–676.
- [17] G. Buffa, L. Fratini, F. Micari, R. Shivpuri, Material Flow in FSW of T-joints: Experimental and Numerical Analysis, *Int. J. Mater. Form.* 1 (2008) 1283–1286. doi:10.1007/s12289-008-0137-6.
- [18] L. Fratini, G. Buffa, F. Micari, R. Shivpuri, On the material flow in FSW of T-joints: Influence of geometrical and technological parameters, *Int. J. Adv. Manuf. Technol.* 44 (2009) 570–578. doi:10.1007/s00170-008-1836-3.
- [19] F. Acerra, G. Buffa, L. Fratini, G. Troiano, On the FSW of AA2024-T4 and AA7075-T6 T-joints: an industrial case study, *Int. J. Adv. Manuf. Technol.* 48 (2009) 1149–1157. doi:10.1007/s00170-009-2344-9.
- [20] K. Krasnowski, Experimental Study of FSW T-joints of EN-AW 6082-T6 and Their Behaviour Under Static Loads, *Arab. J. Sci. Eng.* 39 (2014) 9083–9092. doi:10.1007/s13369-014-1465-0.
- [21] ASM International Handbook Committee, *ASTM Handbook - Volume 2. Properties and Selection: Nonferrous Alloy and Special-Purpose Materials*, 1992.
- [22] A.R. Darvazi, M. Iranmanesh, Prediction of asymmetric transient temperature and longitudinal residual stress in friction stir welding of 304L stainless steel, *Mater. Des.* 55 (2014) 812–820. doi:10.1016/j.matdes.2013.10.030.
- [23] D. Rao, K. Huber, J. Heerens, J.F. dos Santos, N. Huber, Asymmetric mechanical properties and tensile behaviour prediction of aluminium alloy 5083 friction stir welding joints, *Mater. Sci. Eng. A.* 565 (2013) 44–50. doi:10.1016/j.msea.2012.12.014.
- [24] E.E. Feistauer, L.A. Bergmann, L.S. Barreto, J.F. dos Santos, Mechanical behaviour of dissimilar friction stir welded tailor welded blanks in Al-Mg alloys for Marine applications, *Mater. Des.* 59 (2014). doi:10.1016/j.matdes.2014.02.042.
- [25] G.E. Dieter, *Mechanical metallurgy*, New York, McGraw-Hill, 1961.
- [26] J.M. Reed, M.E. Walter, Observations of serration characteristics and acoustic emission during serrated flow of an Al–Mg alloy, *Mater. Sci. Eng. A.* 359 (2003) 1–10. doi:10.1016/S0921-5093(02)00729-3.